Chemical Science

ROYAL SOCIETY OF CHEMISTRY

EDGE ARTICLE

View Article Online
View Journal | View Issue

Cite this: *Chem. Sci.*, 2024, **15**, 3625

All publication charges for this article have been paid for by the Royal Society of Chemistry

A flexible ligand and halogen engineering enable one phosphor-based full-color persistent luminescence in hybrid perovskitoids†

Guowei Xiao,‡ Yu-Juan Ma,‡ Zhenhong Qi, Xiaoyu Fang, Tianhong Chen and Dongpeng Yan *

Received 20th December 2023
Accepted 29th January 2024

DOI: 10.1039/d3sc06845e

rsc.li/chemical-science

Color-tunable room temperature phosphorescent (RTP) materials have raised wide interest due to their potential application in the fields of encryption and anti-counterfeiting. Herein, a series of CdX_2-organic hybrid perovskitoids, (H-apim)CdX_3 and (apim)CdX_2 (denoted as **CdX-apim1** and **CdX-apim2**, apim = 1-(3-aminopropyl)imidazole, X = Cl, Br), were synthesized using apim with both rigid and flexible groups as ligands, which exhibit naked-eye detectable RTP with different durations and colors (from cyan to red) by virtue of different halogen atoms, coordination modes and the coplanar configuration of flexible groups. Interestingly, **CdCl-apim1** and **CdX-apim2** both exhibit excitation wavelength-dependent RTP properties, which can be attributed to the multiple excitation of imidazole/apim, the diverse interactions with halogen atoms, and aggregated state of imidazoles. Structural analysis and theoretical calculations confirm that the aminopropyl groups in **CdCl-apim1** do not participate in luminescence, while those in **CdCl-apim2** are involved in luminescence including both metal/halogen to ligand charge transfer and twisted intramolecular charge transfer. Furthermore, we demonstrate that these perovskitoids can be applied in multi-step anti-counterfeiting, information encryption and smart ink fields. This work not only develops a new type of perovskitoid with full-color persistent luminescence, but also provides new insight into the effect of flexible ligands and halogen engineering on the wide-range modulation of RTP properties.

Introduction

Molecule-based persistent luminescence has emerged as a burgeoning family owing to its application prospects in the fields of optical sensors, anti-counterfeiting, textile industry, *etc.*[1–5] To date, hundreds of such materials have been developed, including single-component organics,[6–9] molecular cocrystals,[10] polymers,[11,12] host–guest systems,[13–15] metal–organic complexes,[16–18] and so on.[19] Mechanisms for persistent luminescence are mainly derived from long-lived room temperature phosphorescence (RTP) and thermal activation delayed fluorescence (TADF). However, according to Kasha's rule, most of the as-reported systems exhibit a monotonous afterglow, which limits their wide applications in multi-color imaging and multichannel information encryption. Therefore, one urgent issue in this field is pursuing a color-adjustable afterglow combining both long lifetime and high efficiency.

Quite recently, the utilization of external stimuli (such as excitation wavelength, force and temperature) has been an effective way to obtain color-tunable afterglow materials, which have attracted increasing attention due to their irreplaceable advantages in anti-counterfeiting applications.[20–25] Up to now, research on multi-color afterglow has achieved some success, and even obtained efficient and long-lived color-tunable RTP in rare materials.[26–31] For example, Huang *et al.* reported a series of full-color RTP elastomers by modifying the chemical structure of monomers;[26] Tao *et al.* achieved full-color RTP in polymer-based materials by doping a series of polycyclic aromatic hydrocarbons.[27] However, the full-color RTP in the reported materials is mostly derived from multiple chromophores, and one phosphor-based materials showing a recognizable afterglow are still limited.[31]

Crystalline metal–organic hybrids (MOHs), as an important branch of molecular RTP materials, have many unique advantages to obtain recognizable persistent luminescence.[18,32–38] By providing a rigid environment and promoting heavy atom effects (HAE), MOHs could achieve long-lived RTP and high-efficiency afterglow simultaneously. The color-tunable persistent luminescence can also be realized by manipulating the

Beijing Key Laboratory of Energy Conversion and Storage Materials and Key Laboratory of Radiopharmaceuticals, Ministry of Education, College of Chemistry, Beijing Normal University, Beijing 100875, P. R. China. E-mail: yandp@bnu.edu.cn

† Electronic supplementary information (ESI) available: Experimental procedures, crystallographic data, theoretical calculations, structural characteristics and measurements of optical properties. CCDC 2253383–2253388. For ESI and crystallographic data in CIF or other electronic format see DOI: https://doi.org/10.1039/d3sc06845e

‡ These authors contributed equally to this work.

coordination mode and molecular configuration.[39–42] For example, terephthalic acid (TPA)-based MOHs can be made to show blue and green afterglows by controlling the distance between neighboring TPA molecules.[39–41] Our group also proved a series of 4-hydroxypyridine-based MOHs showing TADF-dominated blue and RTP-dominated green afterglows, respectively.[42] To date, developing full-color emission in one phosphor-based MOHs is still highly desirable.

Herein, we take the challenge to develop one phosphor based full-color persistent luminescence through the introduction of flexible ligands and engineering of halogen atoms in MOHs. It was reported that molecules with flexible segments present the potential to modulate intermolecular interactions and thus the RTP emission,[43,44] such as molecular rotor-generated ultralong phosphorescence,[43] and flexible ligand-induced dual phosphorescence.[44] In this work, a new series of MOHs, (H-apim)CdX_3 and (apim)CdX_2 (apim = 1-(3-aminopropyl) imidazole; X = Cl, Br; denoted as **CdX-apim1** and **CdX-apim2**), were facilely fabricated using apim as an organic ligand which includes both rigid and flexible units (Scheme 1). For the two MOHs, the Cd centers are six-coordinated with octahedral configurations and form 1D inorganic chains through face/point-sharing in **CdX-apim1** and edge-sharing in **CdX-apim2**, which can both be classified as perovskitoids.[45] Then, decoration/connection by the end-coordinated and bridging-coordinated apim form the final 1D and 2D structures. The four perovskitoids exhibit a multi-color afterglow covering nearly the whole visible region from cyan to red, by regulating the halogen atoms, coordination modes, and co-planar configuration of flexible groups. The excitation wavelength-dependent afterglow properties in these perovskitoids can be attributed to the multi-central RTP emissions from both imidazole units and metal/halogen to ligand charge transfer (MLCT/XLCT). Moreover, we have demonstrated that the combination of these perovskitoids shows a wide range of application prospects in multi-step anti-counterfeiting and information encryption fields. Therefore, this work not only develops a new type of low-dimensional MOH based perovskitoids with a wide ranging afterglow emission for information safety, but also provides an efficient strategy combining a rigid and flexible ligand and halogen engineering for one phosphor based full-color luminescence.

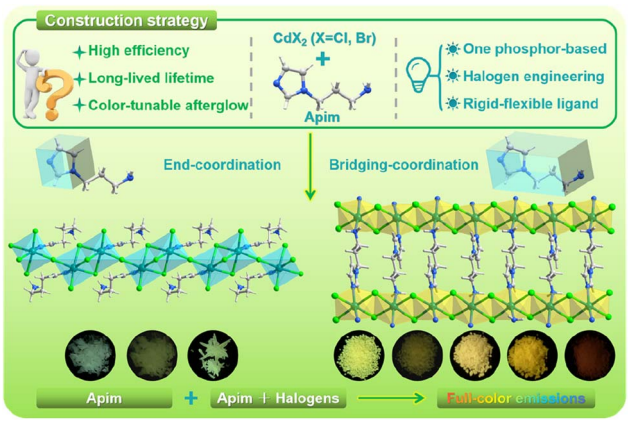

Scheme 1 Construction strategy and one ligand-based perovskitoids with a multicolor afterglow ranging from cyan to red.

Results and discussion

Through a hydrothermal reaction under acid conditions, with the initial molar ratio of CdX_2 to apim of 1 : 2, the **CdX-apim1** can be obtained. Single crystal X-ray diffraction (SCXRD) data reveal that **CdCl-apim1** and **CdBr-apim1** are isostructural with the monoclinic space group *P*2/*c* (no. 13). Taking **CdCl-apim1** as an example, its asymmetric unit contains one Cd^{2+} ion, three Cl^- anions, and one protonated H-apim ligand (Fig. 1a). Cd centers are six-coordinated with an octahedral configuration, which is surrounded by the coordination of one N-atom from apim ligands, four bridging Cl^- anions and one end-coordinating Cl^- anion. The face/point-sharing octahedrons form a 1D chain through bridging Cl^- anions, and apim ligands and Cl1 are decorated on the chain as end ligands (Fig. 1b). Each chain still contains π···π interactions between adjacent apim ligands, which could not only increase their structural stability, but also possibly trigger the photoemission of aggregated states (Fig. 1c). Neighboring chains have further constructed a three-dimensional supramolecular structure through N–H···Cl interactions (Fig. 1d). The Cd–N bond length is 2.253(6) Å, while the Cd–Cl bond lengths are in the range of 2.5674(16)–2.7157(17) Å; the bond angles around the Cd centers range from 80.42(4) to 174.50(4). More details of bonding parameters are listed in Table S2.†

By alternation of the initial molar ratio of CdX_2 to apim from 1 : 2 to 1 : 4 and 1 : 3, new forms of perovskitoids (**CdCl-apim2** and **CdBr-apim2**) can be obtained, which are isostructural with the monoclinic space group $P2_1/c$ (no. 14) at 100 K. For **CdCl-apim2**, its asymmetric unit contains one Cd^{2+} ion, two Cl^- anions, and one apim ligand (Fig. 2a). Cd centers are six-coordinated with an octahedral configuration, which is surrounded by the coordination of two N-atoms from apim ligands and four bridging Cl^- anions. The edge-sharing octahedrons form a chain through bridging Cl^- anions, and apim ligands as pillars link adjacent chains constructing a 2D layer (Fig. 2b and

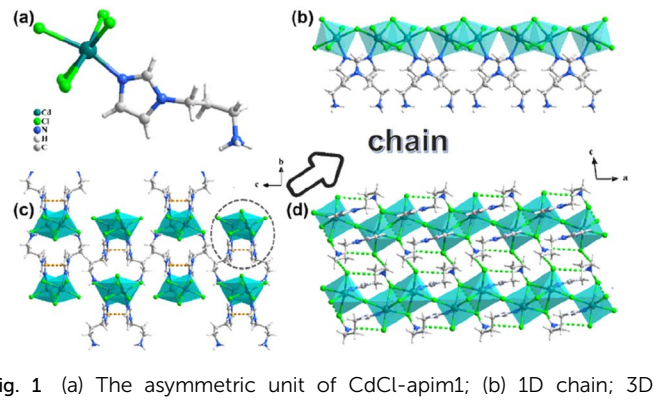

Fig. 1 (a) The asymmetric unit of CdCl-apim1; (b) 1D chain; 3D supramolecular structure along the *a* axis (c) and *b* axis (d) (orange dashed lines: π···π interactions; Green dashed lines: N–H···Cl).

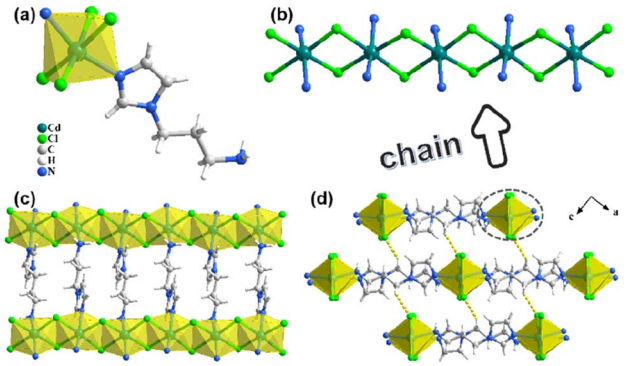

Fig. 2 (a) The asymmetric unit of **CdCl-apim2**; (b) 1D chain; (c) 2D layer; (d) 3D supramolecular structure along the *b* axis (yellow dashed lines: C–H···Cl).

c). Each layer still contains N–H···Cl and C–H···π interactions (Fig. S2†), and neighboring layers construct a three-dimensional structure through weak C–H···Cl interactions (Fig. 2d). Interestingly, different from that of **CdX-apim1**, the phase transformation occurs at 282 K for **CdX-apim2**. With temperature increasing, the space group of **CdCl-apim2** transforms to $P2_1/m$ and the asymmetric unit shrinks to half, while the coordination modes and stacking modes are almost unchanged. Continuous shape measurement analyses were performed by SHAPE 2.0 Software to clarify the geometrical configuration of the Cd^{2+} centers at different temperatures, showing that octahedrons tend to transform to irregular octahedrons at 282 K (Table S4†). At 100 K, the Cd–N bond lengths are in the range of 2.284(8)–2.298(9) Å, while the Cd–Cl bond lengths are in the range of 2.586(2)–2.787(2) Å. The shortest intrachain and interchain Cd···Cd distances are 3.846 and 11.560 Å, respectively. The bond angles around the Cd centers range from 77.9(2) to 175.22(4). At 282 K, the Cd–N bond lengths are in the range of 2.272(8)–2.298(10) Å, while the Cd–Cl bond lengths are in the range of 2.5844(19)–2.829(2) Å. The shortest intrachain and interchain Cd···Cd distances are 3.893 and 11.530 Å, respectively. The bond angles around the Cd centers range from 77.83(18) to 174.66(3). All details are listed in Tables S5 and S6.†

The experimental PXRD data are also consistent with the curves derived from SCXRD data, suggesting the high purity of the crystalline phases (Fig. S3 and S4†). For **CdX-apim2**, the two simulated curves of one compound derived from SCXRD data at different temperatures show some differences, which corresponds to the phase transition process. The TGA plots for the four compounds in Fig. S5† show that there is no weight loss below 250 °C, which proves that all compounds have good thermal stability.

CdCl-apim1 exhibits blue photoluminescence (PL) under 365 nm UV light (Fig. 3a), and its prompt spectrum in Fig. 3b and S6a† shows one emission band at 395 nm with the lifetime of 6.83 ns and the photoluminescence quantum yield (PLQY) of 11.4% (Fig. 3c and S7,† $\lambda_{ex} = 330$ nm), which can be assigned to fluorescence. To identify the origin of PL, the prompt spectra of the pristine apim diluted with water and ethanol were derived (10^{-6} M, Fig. S8†), respectively. The spectra show that the emission bands are both located at 395 nm, and are associated with the fluorescence peak of **CdX-apim1**. This suggests that the luminescence of **CdX-apim1** is generated from the imidazole parts because the emission of the aminopropyl group can be basically ignored in solution.[29–36] After removing the 365 and 395 nm UV lamp, **CdCl-apim1** shows cyan and yellow emission, respectively, exhibiting excitation wavelength-dependent afterglow properties. As shown in Fig. 3d and S9,† the emission peak (delay 1 ms) moves from 480 nm to 530 nm with the excitation wavelength changing from 280 to 360 nm, and the corresponding CIE coordinates shift from cyan (0.239, 0.335) to

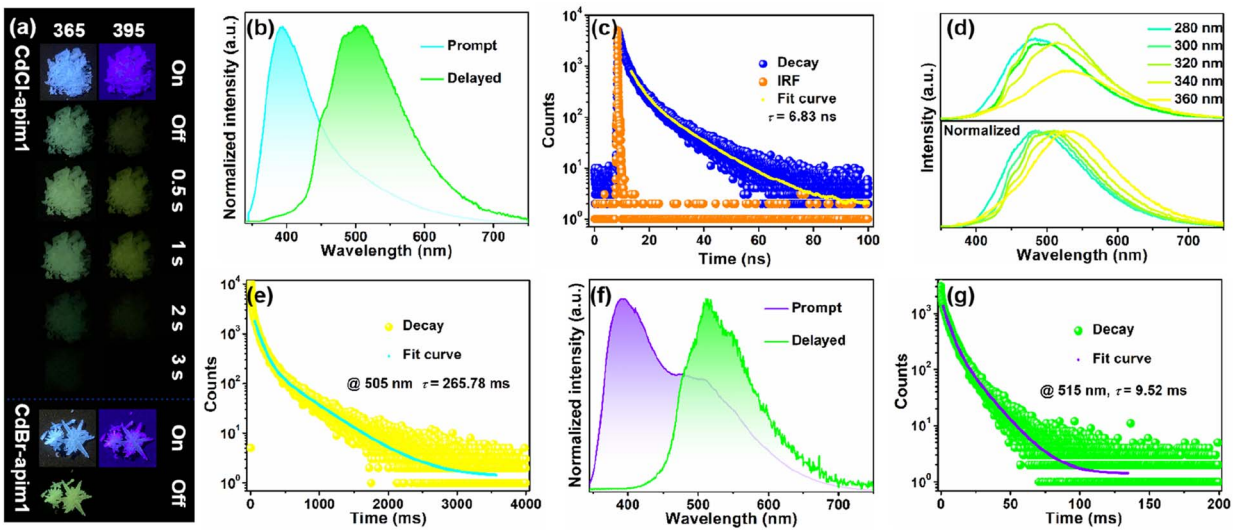

Fig. 3 (a) Photographs of **CdCl-apim1** and **CdBr-apim1** before and after removing the 365/395 nm UV lamp; the prompt and delayed spectra of **CdCl-apim1** (b) and **CdBr-apim1** (f); (c) fluorescence decay profile of **CdCl-apim1**; (d) delayed spectra of **CdCl-apim1** excited by different wavelengths; phosphorescence decay profiles of **CdCl-apim1** (e) and **CdBr-apim1** (g).

yellow-green (0.323, 0.441). The emission at 480 nm can be assigned to the imidazole group of apim, while the emission at >480 nm could be assigned to its interactions with halogen atoms and/or aggregated state of imidazoles.[46] Among them, the emission band is located at 505 nm when excited by the optimal excitation wavelength (330 nm), and the decay curve monitored at 505 nm in Fig. 3e indicates that its triplet lifetime is 265.78 ms. On the one hand, the long lifetime can be attributed to the external HAE of Cd^{2+} and Cl^{-}, which effectively promotes intersystem crossing (ISC). On the other hand, the strong coordinate bonds between imidazole and Cd^{2+} synergizing with the hydrogen bonds between protonated amino and halogens create a relatively rigid environment for apim, which reduces nonradiative transitions effectively.

CdBr-apim1 exhibits cyan emission under 365 nm UV light and a fleeting green-yellow afterglow after removing the UV lamp. The prompt spectrum of **CdBr-apim1** in Fig. 3f and S6b† shows two emission bands at 395 nm and 515 nm with the PLQY of 6.2% (λ_{ex} = 330 nm). The former can be assigned to fluorescence while the latter can be classified as RTP, and the stronger RTP in the prompt spectrum can be due to the stronger HAE of Br^{-} ions. The decay curves for the two emissions exhibit a singlet lifetime of 4.12 ns and triplet lifetime of 9.52 ms (Fig. 3g and S10†).

CdCl-apim2 exhibits both reverse (λ_{ex} = 300–360 nm) and forward (λ_{ex} = 360–540 nm) wavelength-dependent PL properties at room temperature. As shown in Fig. 4b and S11,† the prompt spectra show one emission band at about 500 nm when excited by 300 nm UV light; with the excitation wavelength moving to 360 nm, the emission band presents a blue shift to 450 nm with a lifetime of 4.80 ns. When the excitation wavelength moves to 420 nm, the intensity strongly enhances and the emission band presents a red shift and is back to 500 nm with the lifetime of 4.93 ns. The similar fluorescence lifetimes support that two emissions (under 300 and 420 nm excitation) are generated from the same singlet state (PLQY: 11.8%, Fig. S12†). As the excitation wavelength increases, the emission can be bathochromically shifted crossing the full-color blue to red region. Furthermore, after removing the 365 or 395 nm UV lamp, **CdCl-apim2** shows a green or yellow afterglow respectively, so the delayed spectra were also exported. As depicted in Fig. 4c and S13,† with the excitation wavelength varying from 300 to 400 nm, the afterglow exhibits an obvious bathochromic shift from green (CIE: 0.325, 0.441) to yellow (CIE: 0.429, 0.466), together with the emission peak changing from 525 to 585 nm. The decay curve in Fig. 4d shows a long lifetime of 329.31 ms after excitation with 350 nm UV light. Compared with the pure apim, the enhanced lifetime can be attributed to two factors: (a) the introduction of heavy atoms enhances the spin–orbit coupling (SOC) and increases the probability of ISC; (b) strong coordinate bonds fix apim molecules in the rigid crystalline environment and reduce nonradiative transitions.

By replacing the Cl^{-} with Br^{-}, **CdBr-apim2** also exhibits reverse (λ_{ex} = 325–405 nm) and forward (λ_{ex} = 405–545 nm) wavelength-dependent PL properties. As shown in Fig. 4e and S14,† the prompt spectra show one emission band at about 520 nm with the lifetime of 4.26 ns when excited by 325 nm UV light. With the excitation wavelength moving to 405 nm, the emission band shifts to 480 nm with the lifetime of 3.92 ns and the PLQY of 17.9%. With the excitation wavelength moving to 445 nm, the intensity strongly enhances and the emission band is back to 520 nm with the lifetime of 4.15 ns. As the excitation wavelength increases, the emission ranges from the blue to red full-color visible region. It is worth mentioning that **CdBr-apim2** can exhibit yellow, orange, and even red afterglows after removing the 365 nm, 395 nm, and white-light lamps, respectively. As depicted in Fig. 2f and S15,† with the excitation wavelength varying from 345 to 465 nm, the afterglow exhibits an obvious bathochromic shift from yellow-green (CIE: 0.386, 0.496) to red (CIE: 0.578, 0.409) accompanied by the emission peak changing from 540 to 630 nm. The decay curve in Fig. 2g

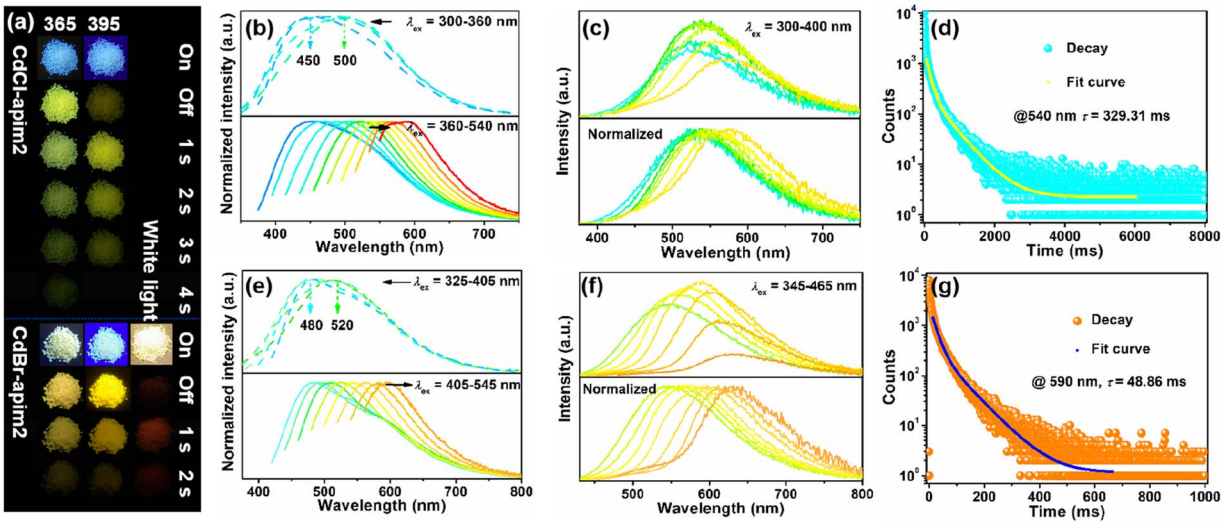

Fig. 4 (a) Photographs of **CdCl-apim2** and **CdBr-apim2** before and after removing the 365/395 nm UV lamp or white-light lamp; the prompt (b) and delayed (c) spectra of **CdCl-apim2** excited by different wavelengths; the prompt (e) and delayed (f) spectra of **CdBr-apim2** excited by different wavelengths; phosphorescence decay profiles of **CdCl-apim2** (d) and **CdBr-apim2** (g).

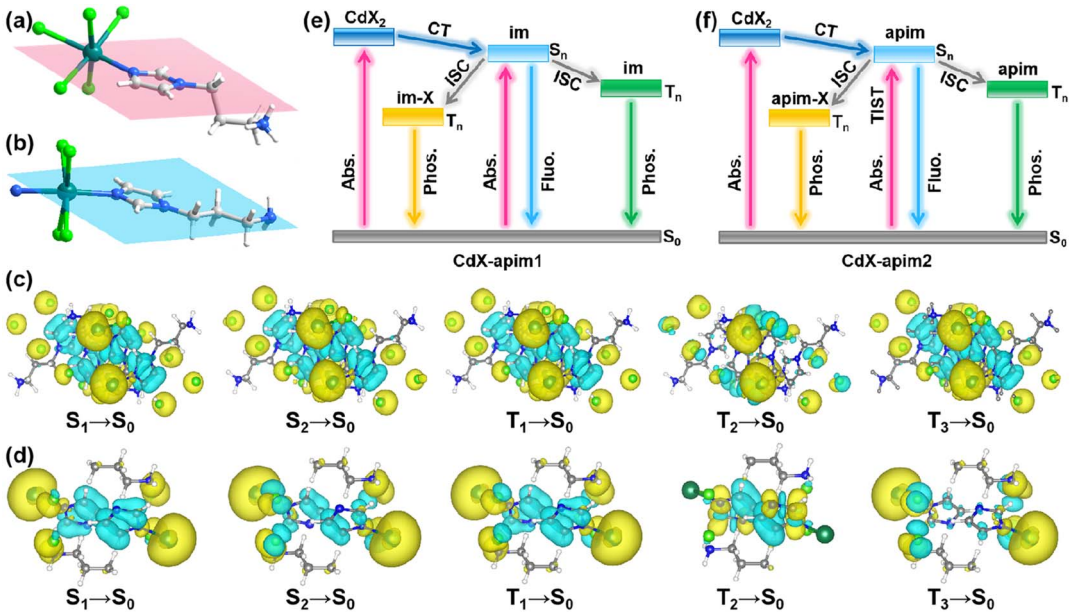

Fig. 5 The crystal structures of **CdCl-apim1** (a) and **CdCl-apim2** (b); distribution maps of the hole and electron of $S_1 \rightarrow S_0$ and $T_n \rightarrow S_0$ transitions in **CdCl-apim1** (c) and **CdCl-apim2** (d) (yellow, hole; cyan, electron-accepting part); the photophysical processes for **CdX-apim1** (e) and **CdX-apim2** (f); abs., absorption; fluo., fluorescence; phos., phosphorescence.

shows the longest afterglow lifetime of 48.86 ms ($\lambda_{ex} = 405$ nm). The wavelength-dependent emissions for **CdX-apim2** can be attributed to multiple emission centers, which include the emission from apim ligands, and those from interactions between the ligands and halogen ions.

To further understand the luminescence properties, we employed **CdBr-apim2** as an example to export a series of temperature-dependent emission spectra and decay curves. As shown in Fig. S16,† the PL intensity gradually increases as the temperature decreases under different excitations, which can be attributed to the limitation of non-radiative transitions at low temperatures. When excited by 395 nm UV light, the intensity at 480 nm remains unchanged with the temperature rising from room temperature to 360 K, confirming that the emission at 480 nm can be classified as fluorescence. In addition, when excited by 365 nm, 395 nm, and 405 nm light, the emission at long wavelengths is more sensitive to temperature, indicating that the emissions at long wavelengths are attributed to triplet excitons. Furthermore, the delayed emission spectra and lifetime decay curves show that the intensity gradually increases and the decay rate gradually slows down as the temperature reduces (Fig. S17†), further confirming that the long-lived luminescence can be ascribed to phosphorescence.

The steady-state and delayed emission spectra both exhibit significant changes in intensity between 180 and 260 K, which is related to the fact that **CdBr-apim2** undergoes a phase transition as observed from temperature-dependent SCXRD. To verify this conclusion, we also tested the differential scanning calorimetry (DSC) curves in heating and cooling processes. As shown in Fig. S18,† a pair of endothermic and exothermic peaks appears between 170 and 260 K, confirming the reversible phase transitions in this temperature range.

To investigate the origin of differences in PL between **CdX-apim1** and **CdX-apim2**, we further analyzed the structures of the two perovskitoids. As depicted in Fig. 5a and b, only one C atom is coplanar with the imidazole unit in **CdX-apim1** while all molecules are coplanar in **CdX-apim2**. Planar conformation is beneficial to electron delocalization,[47] and thus the RTP emission in **CdX-apim2** is red-shifted compared to **CdX-apim1**; furthermore, longer lifetime and higher quantum yield can be achieved. In addition, the high-efficiency RTP is also related to the coordination of the aminopropyl group with Cd^{2+} in **CdX-apim2**. Compared to intermolecular interactions in **CdX-apim1**, the coordinate bonds offer a more rigid environment for apim, reducing non-radiative transitions effectively.

To better understand the electronic structures and excited states during the PL process, distribution maps of the hole and electron in typical **CdCl-apim1** and **CdCl-apim2** were exported by density functional theory (DFT) and time-dependent density functional theory (TDDFT) calculations. For **CdCl-apim1** (Fig. 5c and S19†), the electrons mainly distribute in the imidazole parts of apim, while holes mainly distribute in Cd and Cl atoms, suggesting the occurrence of charge transfer from Cd/Cl to the imidazole parts (MLCT and XLCT) during the photoexcitation. For **CdCl-apim2** (Fig. 5d and S20†), the electrons mainly distribute in the imidazole parts while holes mainly distribute in Cd/Cl atoms and aminopropyl groups, proving that not only do the MLCT and XLCT processes occur, but also the twisted intramolecular charge transfer (TICT) exists. Such multifarious and alternative radiative transition modes further explain the forward and reverse excitation wavelength-dependent PL properties of **CdX-apim2**. Corresponding to the experiments, the absorption band located at 200–280 nm can be attributed to the π–π^* transition of the imidazole unit, and the absorption band

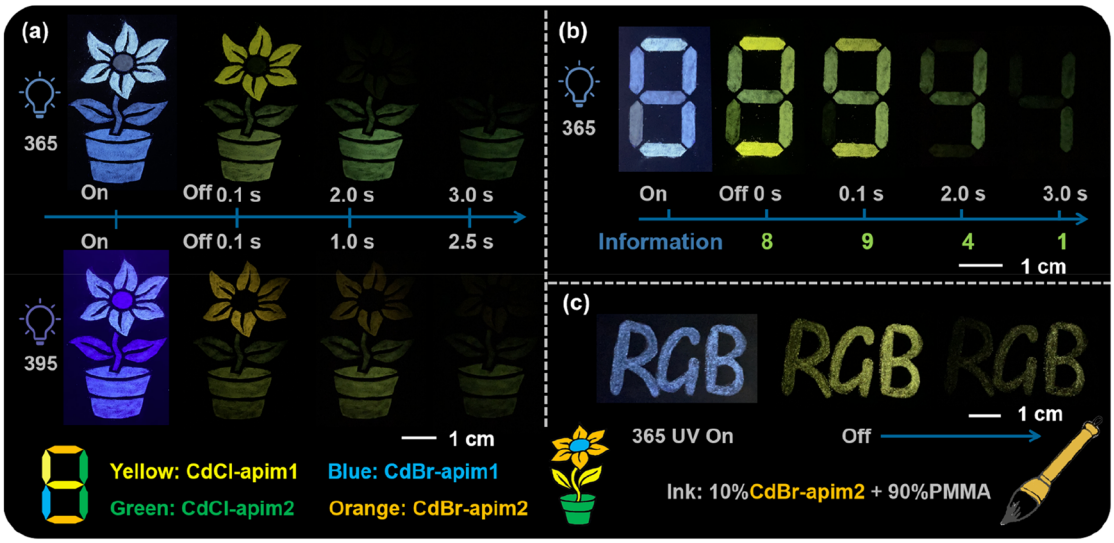

Fig. 6 (a) The photographs of the pattern before and after removing the 365 and 395 nm UV lamp; (b) The "8" model and (c) "RGB" writing in ink before and after removing the 365 UV lamps.

in the 300–500 nm region can be attributed to the n–π* transition based on XLCT (Fig. S21†).[46] **CdX-apim2** exhibits stronger absorption in the range of 300–500 nm compared to **CdX-apim1**, confirming that **CdX-apim2** exhibits stronger n–π* transitions, which corresponds to its stronger RTP. To better describe the excitation wavelength-dependent RTP in these MOH based perovskitoids, we proposed their plausible photophysical processes as shown in Fig. 5e and f, respectively.

The multicolor afterglow properties give these perovskitoid materials prospects in the fields of multi-step anti-counterfeiting and information encryption. Therefore, we constructed a multi-step anti-counterfeiting model as shown in Fig. 6a. When excited by 365 nm UV light, the afterglow of the stamens first disappears, and then those of the petals, leaves, and flowerpots disappear in turn. When excited by 395 nm UV light, the stamens do not exhibit any afterglow, and the afterglow colors of petals, leaves, and flowerpots all move to long wavelengths. Meanwhile, the afterglow of petals and leaves disappears simultaneously due to the difference of the optimal excitation wavelength between **CdBr-apim2** (405 nm) and **CdCl-apim1** (330 nm). That is, when excited by 365 and 395 nm UV light, we can observe distinguishable afterglow phenomena by the naked eye, thus confirming that these materials can be applied in multiple information anti-counterfeiting fields. Currently, verification codes or passwords are mostly composed of four digits, so we also designed the digital "8" model to demonstrate the application prospects of these MOHs in the field of multiple information encryption and communications. As shown in Fig. 6b, we can observe the number "8" under a 365 nm UV lamp. After turning off the UV lamp, the numbers "8", "9", "4", and "1" can be clearly recognized in turn due to the different afterglow durations, thereby obtaining the correct information "8941" and confirming the advantages in dynamic number encryption. Furthermore, we made a new type of ink using 10% **CdBr-apim2** and 90% poly(-methylmethacrylate) (PMMA) by virtue of their good stability and dispersion (Fig. 6c and S22†). The text written by this ink can still show a legible afterglow after turning off the UV light, which also proves the wide application potential of the materials.

Conclusions

In summary, a series of low-dimensional perovskitoids with full-color photoemission were constructed employing one phosphor (apim) with both rigid and flexible groups as ligands. The four new perovskitoids exhibit a naked-eye detectable long afterglow, in which the different duration times and colors can be highly modulated through engineering halogen atoms, coordination self-assembly modes, and the coplanar configuration of flexible groups. Structural analysis proves that only one C atom is coplanar with imidazole in **CdX-apim1** while all molecules are coplanar in **CdX-apim2**, suggesting that the conformation in **CdX-apim2** is more beneficial to electron delocalization and participation of aminopropyl groups in PL. Theoretical calculations confirm the occurrence of MLCT and XLCT processes in **CdCl-apim1** while MLCT, XLCT, and TICT appear in **CdCl-apim2**, which endows **CdX-apim2** with both forward and reverse excitation wavelength-dependent PL properties as observed in the experiments. Moreover, a multi-step anti-counterfeiting model, information encryption model and new ink have been designed using these one-phosphor based perovskitoids, confirming the promising application prospects of such materials. Therefore, this work not only reports a series of long-lived RTP perovskitoids with a wide emission color range, but also illustrates the influence of the rigid and flexible groups on persistent luminescence from both experimental and theoretical perspectives, which provides a new insight for the design of one phosphor-based multicolor afterglow materials.

Data availability

Experimental procedures, details of the calculations, and additional data can be found in the ESI.†

Author contributions

G. Xiao and Y.-J. Ma contributed equally to this work. D. Yan, G. Xiao and Y.-J. Ma designed the project. G. Xiao and Y.-J. Ma synthesized the samples and carried out the measurements. All authors analyzed the experimental data. G. Xiao, Y.-J. Ma and D. Yan co-wrote the manuscript.

Conflicts of interest

There are no conflicts to declare.

Acknowledgements

This work was supported by the National Natural Science Foundation of China (Grant no. 22275021), the Beijing Nova Program (Grant no. 20230484414), the Beijing Municipal Natural Science Foundation (Grant no. L234064) and the Fundamental Research Funds for the Central Universities.

References

1 T. Maldiney, A. Bessière, J. Seguin, E. Teston, S. K. Sharma, B. Viana, A. J. J. Bos, P. Dorenbos, M. Bessodes, D. Gourier, D. Scherman and C. Richard, *Nat. Mater.*, 2014, **13**, 418–426.
2 W.-L. Zhou, Y. Chen, Q. Yu, H. Zhang, Z.-X. Liu, X.-Y. Dai, J.-J. Li and Y. Liu, *Nat. Commun.*, 2020, **11**, 4655.
3 W. Li, Z. Li, C. Si, M. Y. Wong, K. Jinnai, A. K. Gupta, R. Kabe, C. Adachi, W. Huang, E. Zysman-Colman and I. D. W. Samuel, *Adv. Mater.*, 2020, **32**, 2003911.
4 Y. Yu, M. S. Kwon, J. Jung, Y. Zeng, M. Kim, K. Chung, J. Gierschner, J. H. Youk, S. M. Borisov and J. Kim, *Angew. Chem., Int. Ed.*, 2017, **56**, 16207–16211.
5 X. Zhang, Y. Cheng, J. You, J. Zhang, C. Yin and J. Zhang, *Nat. Commun.*, 2022, **13**, 1117.
6 P. Alam, T. S. Cheung, N. L. C. Leung, J. Zhang, J. Guo, L. Du, R. T. K. Kwok, J. W. Y. Lam, Z. Zeng, D. L. Phillips, H. H. Y. Sung, I. D. Williams and B. Z. Tang, *J. Am. Chem. Soc.*, 2022, **144**, 3050–3062.
7 J. Yuan, R. Chen, X. Tang, Y. Tao, S. Xu, L. Jin, C. Chen, X. Zhou, C. Zheng and W. Huang, *Chem. Sci.*, 2019, **10**, 5031–5038.
8 L. Ma, Q. Xu, S. Sun, B. Ding, Z. Huang, X. Ma and H. Tian, *Angew. Chem., Int. Ed.*, 2022, **61**, e202115748.
9 D. R. Lee, K. H. Lee, W. Shao, C. L. Kim, J. Kim and J. Y. Lee, *Chem. Mater.*, 2020, **32**, 2583–2592.
10 W. Chen, Z. Tian, Y. Li, Y. Jiang, M. Liu and P. Duan, *Chem. – Eur. J.*, 2018, **24**, 17444–17448.
11 Y. Zhang, X. Chen, J. Xu, Q. Zhang, L. Gao, Z. Wang, L. Qu, K. Wang, Y. Li, Z. Cai, Y. Zhao and C. Yang, *J. Am. Chem. Soc.*, 2022, **144**, 6107–6117.
12 X. Zhang, M. Zeng, Y. Zhang, C. Zhang, Z. Gao, F. He, X. Xue, H. Li, P. Li, G. Xie, H. Li, X. Zhang, N. Guo, H. Cheng, A. Luo, W. Zhao, Y. Zhang, Y. Tao, R. Chen and W. Huang, *Nat. Commun.*, 2023, **14**, 475.
13 S. Hirata, K. Totani, J. Zhang, T. Yamashita, H. Kaji, S. R. Marder, T. Watanabe and C. Adachi, *Adv. Funct. Mater.*, 2013, **23**, 3386–3397.
14 Y. Wang, H. Gao, J. Yang, M. Fang, D. Ding, B. Z. Tang and Z. Li, *Adv. Mater.*, 2021, **33**, 2007811.
15 X. Xu and B. Yan, *Adv. Opt. Mater.*, 2022, **10**, 2200451.
16 B. Zhou, Z. Qi, M. Dai, C. Xing and D. Yan, *Angew. Chem., Int. Ed.*, 2023, **62**, e202309913.
17 P. Leo, G. Orcajo, J. A. García, A. M. Ortuño, J. M. Cuerva, D. Briones, G. Calleja, A. Rodríguez-Diéguez, R. Sanz, J. Cepeda and F. Martínez, *J. Mater. Chem. C*, 2021, **9**, 5544–5553.
18 P.-Y. Fu, S.-Z. Yi, Z.-H. Wang, J.-Y. Zhuang, Q.-S. Zhang, J.-T. Mo, S.-C. Wang, H. Zheng, M. Pan and C.-Y. Su, *Angew. Chem., Int. Ed.*, 2023, **62**, e202309172.
19 F. Nie, K.-Z. Wang and D. Yan, *Nat. Commun.*, 2023, **14**, 1654.
20 X. Zhang, K. C. Chong, Z. Xie and B. Liu, *Angew. Chem., Int. Ed.*, 2023, **62**, e202310335.
21 G. Xiao, B. Zhou, X. Fang and D. Yan, *Research*, 2021, **2021**, 9862327.
22 C. Si, T. Wang, A. K. Gupta, D. B. Cordes, A. M. Z. Slawin, J. S. Siegel and E. Zysman-Colman, *Angew. Chem., Int. Ed.*, 2023, **62**, e202309718.
23 Z. Chen, X. Chen, D. Ma, Z. Mao, J. Zhao and Z. Chi, *J. Am. Chem. Soc.*, 2023, **145**, 16748–16759.
24 L. Zhang and P. Naumov, *Angew. Chem., Int. Ed.*, 2015, **54**, 8642–8647.
25 S. Feng, Y. Ma, S. Wang, S. Gao, Q. Huang, H. Zhen, D. Yan, Q. Ling and Z. Lin, *Angew. Chem., Int. Ed.*, 2022, **62**, e202116511.
26 J. Wei, M. Zhu, T. Du, J. Li, P. Dai, C. Liu, J. Duan, S. Liu, X. Zhou, S. Zhang, L. Guo, H. Wang, Y. Ma, W. Huang and Q. Zhao, *Nat. Commun.*, 2023, **14**, 4839.
27 X. Zheng, Q. Han, Q. Lin, C. Li, J. Jiang, Q. Guo, X. Ye, W. Z. Yuan, Y. Liu and X. Tao, *Mater. Horiz.*, 2023, **10**, 197–208.
28 Y. Zuo, H. Yang, K. Wang, Y. Song, L. Jiang, W. Huang, X. Xue, Q. Jiang, B. Jiang and G. Zhang, *Macromolecules*, 2023, **56**, 5854–5864.
29 Q. Zhou, T. Yang, Z. Zhong, F. Kausar, Z. Wang, Y. Zhang and W. Z. Yuan, *Chem. Sci.*, 2020, **11**, 2926–2933.
30 S. Feng, Q. Huang, S. Yang, Z. Lin and Q. Ling, *Chem. Sci.*, 2021, **12**, 14451–14458.
31 Y. Mu, F.-Y. Cao, X.-Y. Fang, Z.-X. Liu, J.-Q. Wang, S.-D. Han, J. Pan, Q. Wei, J.-H. Li and G.-M. Wang, *Adv. Opt. Mater.*, 2022, **11**, 2202402.
32 B. Zhou and D. Yan, *Chem. Sci.*, 2022, **13**, 7429–7436.
33 S. Wang, Y.-J. Shi, S. Chen, Z. Lin, Z. Jiang, W.-M. Liao and J. He, *Chem. Mater.*, 2023, **35**, 3015–3023.
34 H.-X. Wu, X.-M. Lu, J.-Y. Chen, X.-G. Yang, W.-J. Qin and L.-F. Ma, *Inorg. Chem.*, 2021, **60**, 846–851.
35 Y.-J. Ma, X. Fang, G. Xiao and D. Yan, *Angew. Chem., Int. Ed.*, 2022, **61**, e202114100.
36 T. Chen, Y.-J. Ma and D. Yan, *Adv. Funct. Mater.*, 2023, **33**, 2214962.

37 P. Leo, D. Briones, J. A. García, J. Cepeda, G. Orcajo, G. Calleja, A. Rodríguez-Dieguez and F. Martínez, *Inorg. Chem.*, 2020, **59**, 18432–18443.
38 J.-H. Wei, W.-T. Ou, J.-B. Luo and D.-B. Kuang, *Angew. Chem., Int. Ed.*, 2022, **61**, e202207985.
39 S. Kuno, H. Akeno, H. Ohtani and H. Yuasa, *Phys. Chem. Chem. Phys.*, 2015, **17**, 15989–15995.
40 X. Yang and D. Yan, *Adv. Opt. Mater.*, 2016, **4**, 897–905.
41 H. Liu, W. Ye, Y. Mu, H. Ma, A. Lv, S. Han, H. Shi, J. Li, Z. An, G. Wang and W. Huang, *Adv. Mater.*, 2022, **34**, 2107612.
42 B. Zhou, G. Xiao and D. Yan, *Adv. Mater.*, 2021, **33**, 2007571.
43 L. Gu, H. Shi, M. Gu, K. Ling, H. Ma, S. Cai, L. Song, C. Ma, H. Li, G. Xing, X. Hang, J. Li, Y. Gao, W. Yao, Z. Shuai, Z. An, X. Liu and W. Huang, *Angew. Chem., Int. Ed.*, 2018, **57**, 8425–8431.
44 F.-Y. Cao, H.-H. Liu, Y. Mu, Z.-Z. Xue, J.-H. Li and G.-M. Wang, *J. Phys. Chem. Lett.*, 2022, **13**, 6975–6980.
45 I. Spanopoulos, I. Hadar, W. Ke, P. Guo, S. Sidhik, M. Kepenekian, J. Even, A. D. Mohite, R. D. Schaller and M. G. Kanatzidis, *J. Am. Chem. Soc.*, 2020, **142**, 9028–9038.
46 Y.-J. Ma, Z. Qi, G. Xiao, X. Fang and D. Yan, *Inorg. Chem.*, 2022, **61**, 16477–16483.
47 Z. Zhao, Y. Li, X. Chen, Y. Zhang and W. Z. Yuan, *Chem. Commun.*, 2022, **58**, 545–548.